RSC Advances

ROYAL SOCIETY OF CHEMISTRY

www.rsc.org/advances

Electrospun Tailored ZnO Nanostructures – Role of Chloride ions

Prabakaran Shankar and John Bosco Balaguru Rayappan*

Nanosensors Lab @Centre for Nanotechnology & Advanced Biomaterials (CeNTAB)

School of Electrical & Electronics Engineering (SEEE)

SASTRA University, Thanjavur – 613 401, India

Graphical Abstract

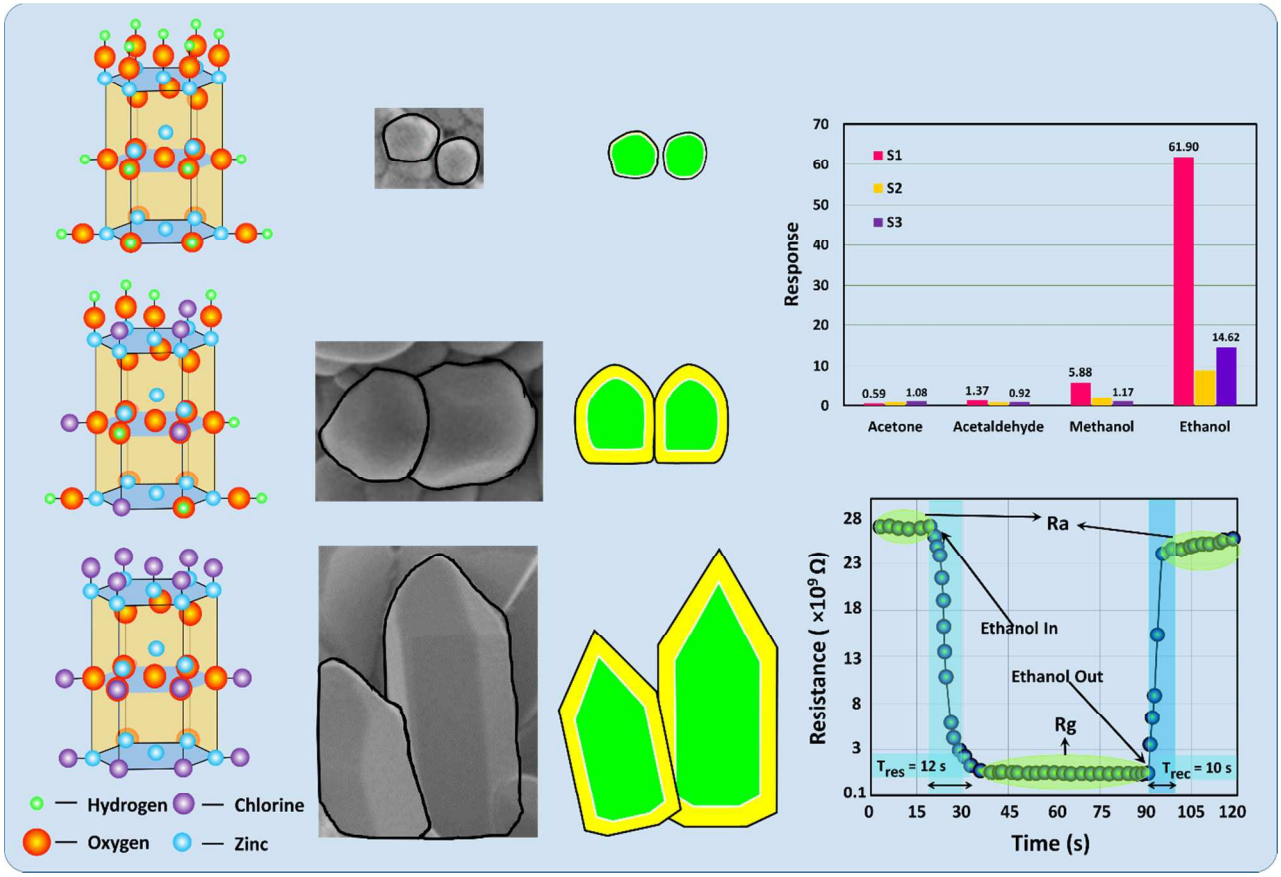

Figure: Role of ligands in tailoring ZnO morphology and ethanol sensing characteristics of ZnO nanosphere

Electrospun Tailored ZnO Nanostructures – Role of Chloride ions

Prabakaran Shankar and John Bosco Balaguru Rayappan*

Nanosensors Lab @ Centre for Nanotechnology & Advanced Biomaterials (CeNTAB)

School of Electrical & Electronics Engineering (SEEE)

SASTRA University, Thanjavur – 613 401, India

***Corresponding author:**

Prof. John Bosco Balaguru Rayappan

School of Electrical & Electronics Engineering (SEEE) &

Centre for Nanotechnology & Advanced Biomaterials (CeNTAB)

SASTRA University, Thanjavur – 613 401, India

Email: rjbosco@ece.sastra.edu (J.B.B Rayappan); madanprabakar@gmail.com (P. Shankar)

Tel.: +91 4362 264101-108 x2255; Fax: +91 4362 264120

Abstract

A novel way of transforming ZnO nanospheres to nanorods using electrospinning technique has been identified as one of the simple methods to control the growth of nanostructures. In this work, ZnO nanospheres and pencil like nanorods were successfully grown using electrospin technique with the precursor solution containing polyvinyl alcohol (PVA) and zinc acetate of desired weight ratio. Also, to control the growth of ZnO nanostructures, chloride ions were used as a capping agent. X-ray diffraction (XRD) pattern confirmed the influence of chloride ion concentration on the growth of ZnO nanostructures. Field emission scanning electron micrographs (FE-SEM) of as-deposited samples showed the formation of uniform and defect free ZnO-PVA composite nanofibers and the calcined samples revealed the growth of nanospherical and pencil like nanorod shaped ZnO. The growth mechanism, electrical characteristics as well as the room temperature ethanol sensing characteristics of the calcined ZnO nanostructures were investigated. The influence of morphology, grain and grain boundary resistances, activation energy of ZnO nanostructures and dissociation bond energy of ethanol molecules on the receptor and transduction functions of ZnO sensing elements has been discussed.

Keywords: Zinc oxide (ZnO), Electrospinning, Nanofibers, Nanorod, Ethanol, Gas sensor

1 Introduction

One-dimensional (1D) or quasi 1D nanostructures are of great interest due to their remarkable physical and chemical properties achieved by cations of different valence states and distinct crystallographic structures.[1] In the recent past, scientists have developed such nanostructures through various chemical[2] and physical[3] processes. Low dimensional nanostructures offer numerous advantages in all the practical applications such as light-emitting diodes, ultraviolet lasers, field emission devices, solar cells, nanogenerators, nanocantilevers and gas sensors[4] due to their high surface area, percolated links, inter-particle boundaries and confinement of electrons in different energy states.

Among many functional semiconducting oxides[5], hexagonal wurtzite structured ZnO material has diverse nanostructures and exhibits dual semiconducting and piezoelectric properties. Tetrahedrally coordinated and alternately stacked O^{2-} and Zn^{2+} ions along the c-axis in the wurtzite structured ZnO crystal favoured the formation of polar plane with Zn^{2+} lattice points in one end and O^{2-} in other end.[6] In recent time, growth of ZnO nanorods, nanotubes, nanowires with polar planes and low aspect ratio has gained much attention in the development of electronic, optoelectronic and energy devices.[6,7] Significantly, morphology of ZnO nanomaterial can be tuned by varying the polar-to-nonpolar facets ratios. The metastable, chemically active polar face (001) and most stable chemically inert non-polar face (100) are the major deciding factors in growing the different ZnO nanostructures.[8,9]

Often, crystal growth habits can be modified by controlling the adsorption of organic surfactants or additives or capping agents like hexamine, oleic acid, citric acid, sodium dodecyl sulfate

(SDS), triethanolamine, hexamethylenetetramine (HMTA) and cetyltrimethylammonium bromide (CTAB) on the seed crystal facets. These organic surfactants have been used to modify the chemical kinetics in-turn influence the nanoparticle surface to assembly behaviours following the oriented attachment mechanism.[10] Also, it influences the growth rate of different plane orientations in a polycrystalline material.[11–13] Huang *et al.*[14] has pointed out the challenge of controlling the ratio of ZnO polar facets to grow nanostructures using organic surfactants.

In this context, Smith *et al.* [15] investigated the role of chloride ions as a structure directing agent in tuning the SnO_2 morphologies. The adsorption of polar molecule namely HCl on the SnO_2 unit cell increased the growth rate. But beyond a certain concentration (0.2 mol L^{-1}) the growth rate was decreased and yielded charged SnO_2 molecules. In the same line, Dedova *et al.*[16] noted the use of HCl as an alternative way to synthesize ZnO nanorod layers. Mani *et al.* [17] investigated the influence of the precursor containing acetate, chloride and nitrate to synthesize ZnO nanorods. Chloride ions in the solution located on each top corner of tetrahedron shaped Zn^{2+} and promoted the growth of hexagonal faceted nanorods perpendicular to the substrate but with flat top morphology. Zhu *et al.* [18] have developed SnO_2/ZnO nano-heterostructures as anode electrode materials for lithium ion batteries. In this work, zinc acetate dihydrate and tin dichloride dihydrate were used as the precursor to synthesis SnO_2 nanorods on the ZnO nanofibers. In this case, the HCl product produced in the precursor solution acted as the capping agent for the growth of SnO_2 nanorods. All these works highlighted the significant role of chloride ions in controlling the growth rate and chemical nature of molecules participating in the growth of highly c-axis oriented ZnO nanostructures.

Template assisted and template free processes have been adapted to synthesize and tailor 1D nanostructures employing hydrothermal, solvothermal, electrodeposition, anode oxide and sonochemical techniques.[14,19–21] Electrospinning (ES) technique has been predominantly used to fabricate 1D nanofibers and has gained much attention during the last decade in the nano arena. In this method, wide range of polymers[22] along with the inorganic salts have been used to develop nanostructures. The major control parameters involved in the synthesis of nanofibers are type of polymer, concentration of polymer, type of solvent, conductivity and feeding rate of the precursor solution[23]. Furthermore, the calcination temperature plays a vital role in optimizing the structural and transport properties of nanofibers.[24] Zhu *et al.* [25] have developed ZnO hollow spheres using electrospun technique with zinc acetate dehydrate and polyvinyl pyrrolidone as precursors. The role of annealing temperature towards the formation of ZnO hollow nanospheres was investigated and concluded that formation of ZnO self-assembly process. Li *et al.*[26] have developed ethanol sensor using ZnO-SnO_2 core shell nanofibers which can detect 100 ppm concentration at 200 °C. Huang *et al.*[27] structurally modified the ZnO nanofibers with indium towards the detection of higher concentration of ethanol at 275 °C. Though such structural and morphological modifications can be used to develop ethanol sensors, further investigations are required to develop room temperature sensors in-turn to reduce the additional power to activate the surface towards adsorption and desorption of target gas molecules in ambient temperature. With this background, fabrication of ZnO nanostructures using ES method has been considered to develop room temperature ethanol sensor. To investigate the influence of electron confinement factor on the sensing performance, a novel but simple capping agent namely chloride ions were used to transform ZnO nanostructure from spherical to rod shape through the

modulated growth of unstable polar and stable non-polar faces. Also, the ethanol sensing properties of synthesised nanostructures like nanoparticles and nanorods have been reported. To the best of our knowledge, this is the novel facile approach and first report on the ES synthesized ZnO nanosphere and nanorod as ethanol sensor.

2 Materials and methods

2.1 Preparation of nanomaterials

ZnO nanofibers were synthesized using an electrospinning equipment with the precursor source of zinc acetate dihydrate ($Zn(CH_3COO)_2 \cdot 2H_2O$) (Sigma Aldrich, $M_w = 219.61$ g mol^{-1}) and poly-vinyl alcohol ($[CH_2CH(OH)]_n$) (M_w = 14,000 g mol^{-1}) of 1 g each. Precursor solution was prepared in different batches with varying hydrochloric acid (HCl) volume of 0, 250 and 500 µL in 10 mL deionised water. The schematic representation of ES equipment setup is shown in supplementary file (Fig. T1). The well dissolved precursor solution was loaded in a 5 mL glass syringe equipped with a needle size of 24 Guage. The needle was connected with a high voltage power supply (15 kV) (Zeonics, Bangalore) and kept at a distance of 12 cm from the collector and the flow rate of 0.01 mL min^{-1} was controlled by syringe pump (Kent Scientific, USA). The composite nanofibers were deposited on the aluminium foil attached with the collector. The as-prepared ZnO nanocomposite fibers-mat was subjected to calcination at 600 °C for 3 h to remove the organic materials in-turn to obtain the pure ZnO nanostructures. Based on the thermal behaviour analysis of PVA[28], as-prepared composite nanofibers were calcined at 600°C. As-prepared and calcined samples were labelled as A1 (0 µL of HCl), A2 (250 µL of HCl) and A3 (500 µL of HCl) and S1, S2 and S3 respectively.

2.2 Characterization techniques

X-ray diffractometer (D8 Focus, Bruker, Germany) was used to study the structural characteristics of ZnO samples. The morphological features of the ZnO nanostructures were recorded using a field emission scanning electron microscope (FESEM, JEOL, 6701F, Japan). The electrical properties like carrier concentration and mobility of the calcined ZnO samples were observed using Hall measurement system (HMS 3000, Ecopia, South Korea). Also the activation energy and change in conductivity of the samples were measured in the temperature range from 300 to 523 K using digital picoammeter (SES instruments, India). The grain and grain boundary resistances were measured by employing electrochemical impedance spectrometer (CHI660E, CH Instruments, USA) with platinum wire as counter electrode, Ag/AgCl as reference electrode and sample coated gold working electrode. 0.1 M of potassium hexacyanoferrate (III) was used as electrolyte and the impedance measurements were carried out in the frequency range of 1 MHz to 10 Hz.

Gas sensing measurements were carried out using a home-made gas testing chamber (Supplementary file; Fig. T2) integrated with an electrometer (Keithley 6517A, USA) to measure the resistance variations in the presence and absence of target gas molecules. Static liquid gas distribution method[29] has been used to calculate the liquid volume of the target volatile organic compounds (VOC) (acetone, acetaldehyde, methanol and ethanol) for fixing the desired concentrations vapour as given in the equation,

$$Q = \frac{V\varphi M}{22.4dp} \times 10^{-6} \times \frac{273 + T_R}{273 + T_B} \quad (1)$$

where, Q is the liquid volume of VOC (L), V is the volume of test chamber (L), φ is the required gas volume fraction, M is the molecular weight of the target molecule (g mol^{-1}), d is the specific gravity of the VOC solution (g cm^{-3}), p is the purity of the selected VOC solutions, T_R and T_B are the temperatures at ambient and test chamber (°C) respectively.

2.3 Fabrication of gas sensor

Gas sensing elements were fabricated using the calcined ZnO nanostructures. To measure the gas response, colloids of calcined ZnO nanoparticles were prepared and uniformly deposited on the thoroughly cleaned glass substrates and dried for 1 h. Silver inter-digited electrode (Supplementary file; Fig. T3) was formed on to the glass substrate using DC magnetron sputtering (12" MSPT, HHV, India) to establish the conducting path. A pair of copper wire was pasted on the silver electrodes using highly conducting silver paste. I-V characteristics (Supplementary file; Fig. T4) confirmed the Ohmic contact established between the copper wire and ZnO sample. Sensing response can be calculated from the formula,

$$S_{Reducing\ gas} = \frac{R_a - R_g}{R_g} \times 100 \qquad (2)$$

where, R_a and R_g are the resistances of sensing element in ambient air and target gas atmosphere respectively.

3 Results and discussions

3.1 Morphological studies

Fig. 1 shows the scanning electron micrographs of as-deposited PVA-ZnO nanocomposite fibers with varying chloride ion concentration as well as their respective calcined samples. All the

electrospun nanofibers were found to be linear, smooth, uniform and without bead. The average diameters of the three types of as-deposited PVA-ZnO composite nanofibers were 150, 260 and 290 nm. The micrographs of calcined samples revealed the transformation of morphology from loosely packed nano-spheres to pencil like nanorods as the influence of the increased chloride ion concentration. The growth mechanism is presented in section 3.3 and one can observe the formation of nanospherical grains (Fig. 1(S1)) and subsequently resulted in the growth of truncated trapezohedron shaped morphology with smooth surface and well defined grain boundaries (Fig. 1(S2)). Fig. 1(S3) clearly depicts the formation of pencil like nanorod morphology (cone like structure) having length in the range of 1µm. The growth of densely populated non-uniform nanorods having multiple surface plane with the average surface area of 48.3 cm^2 were observed. The effective surface area (SA) of the nanorod was estimated using the expression[30],

$$SA = \left[\frac{1}{4}\left(3\sqrt{3}\,w^2\right) + 3wl\right] d \qquad (3)$$

where, w and l is the average width and length of the nanorod respectively and d is the number density of the ZnO nanorods (0.86).

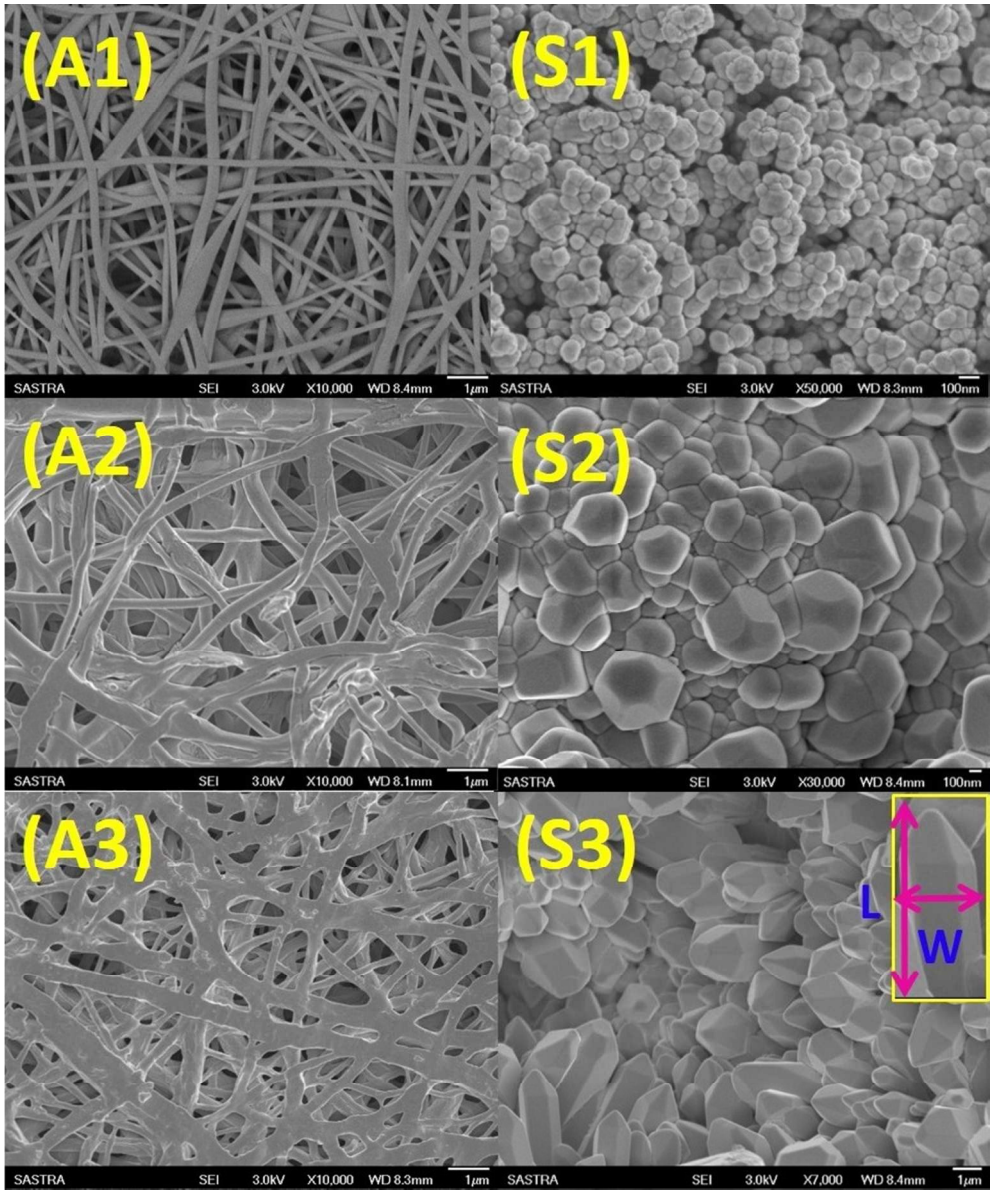

Fig. 1 FE-SEM images of as-deposited ZnO nanofibers (A1, A2 &A3) and calcined samples (S1, S2 & S3), (Inset in S3: Magnified single nanorod).

3.2 Structural studies

XRD patterns of as-deposited and calcined samples are shown in Fig. 2. The as-deposited PVA-ZnO composite fibers showed the diffraction peaks at 14.8°, 17.7° and 26.3° which are related to

the PVA polymer matrix while the absence of other peaks clearly revealed the absence of ZnO crystallites due to the polymerization process.[28] The observation of crystalline peaks for the nanocomposite fibers might be due to the intermolecular hydrogen bonding of PVA monomers.[31] Also, the change in intensity, full-width half maximum and diffraction peak with reference to pure PVA[31] may be emphasized to the intermolecular interaction between the PVA chains and ZnO molecules. As the concentration of chloride ion was increased, new crystalline peaks at 2θ = 22.6°, 25.5°, 31.1°, 34.2°, 37.9°, 44.8° and 54.3° were observed and the same might have resulted due to the formation of ZnO nanostructures. The increase in the intensity of new peaks with chloride ion concentration confirmed the aid of chloride ions toward the formation of ZnO crystallites in the polymer matrix. Evidently, the observed shift in the peak positions at 14.8° and 17.7° for the chloride ions added samples (B & C) clearly confirmed the introduction of disorder in polymer structure as the effect of chlorine ions.

Table 1. Calculated lattice parameters for the calcined samples.

Sample	Plane (1 0 0)		Plane (0 0 2)		d-spacing (Å)	Lattice parameters	
	2Theta (deg.)	FWHM (deg.)	2Theta (deg.)	FWHM (deg.)		c (Å)	a (Å)
S1	32.53	0.4583	34.42	0.1604	2.6061	5.2121	3.1791
S2	32.59	0.1769	35.24	0.1739	2.5477	5.0954	3.1732
S3	32.58	0.2154	35.25	0.1862	2.5465	5.0930	3.1740

Calcined samples showed the diffraction peaks at 32.5°, 34.4°, 37.0° and 56.2° which are attributed to (100), (002), (101) and (110) planes respectively. The observed diffraction pattern is in good agreement with the JCPDS card number 36-1451. The increase in the chloride ion concentration in the precursor lead to the appearance of new peak at 48.3° implied to (102) plane. The increase in peak intensity of (002) plane revealed the influence of Cl ions on the enhanced c-axis growth of ZnO crystal. The calculated lattice parameters of calcined samples (S1, S2 and S3) are listed in Table 1. From these parameters, one can observe the shrinkage of *c* parameter from 5.21 Å to 5.09 Å for the sample S3 which might be attributed to the stress induced *c*-axis compression.[32]

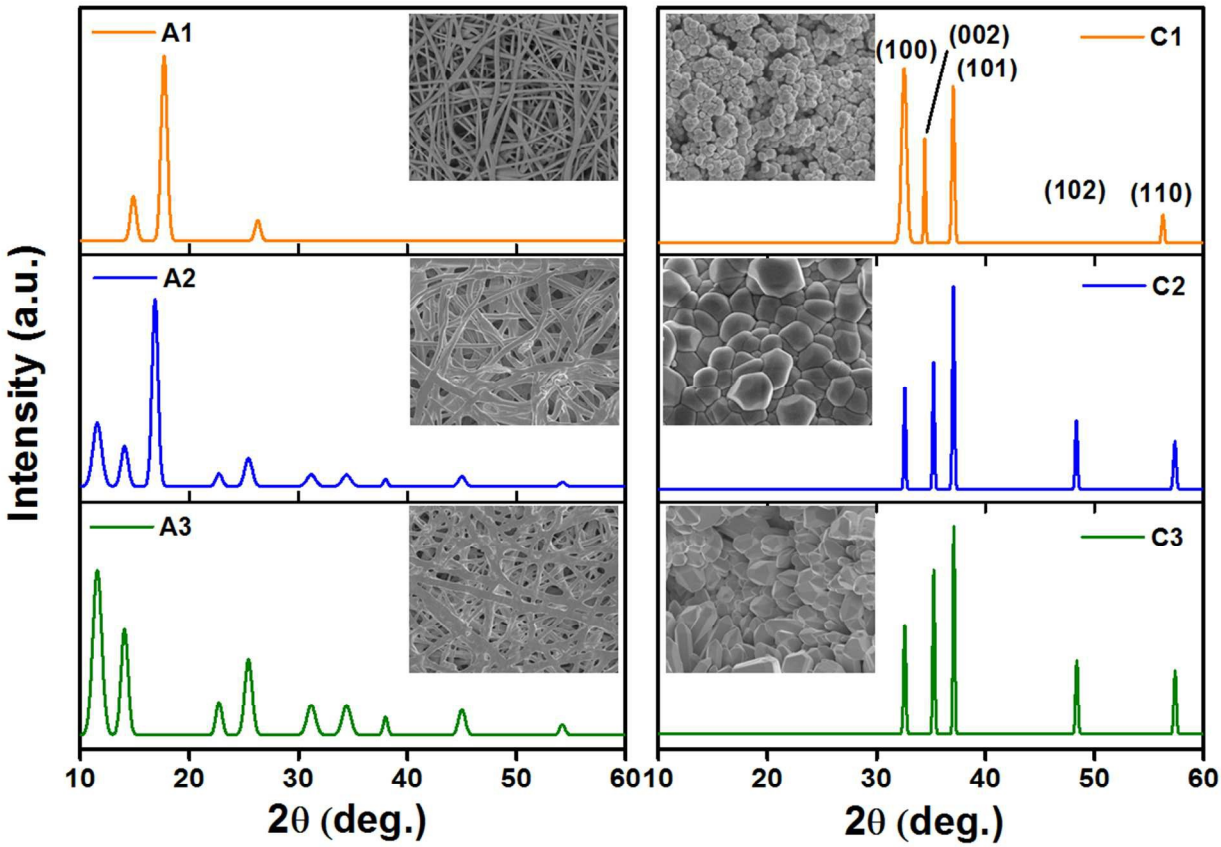

Fig. 2 XRD patterns of as-deposited ZnO nanofibers (A1, A2 & A3) and calcined samples (S1, S2 & S3).

3.3 Growth mechanism

The starting solution with zinc acetate and PVA polymer of specific ratio was subjected to the polymerisation process by stirring the solution for 1 h. During this process, monomer's of PVA were adjoined with the dissociated zinc ions from the coordinated zinc acetate molecules. The observed variation in XRD patterns of pure PVA[31] and PVA mixed with zinc acetate (Fig. 2) confirmed the nanocomposite formation. Further, the formation of ZnO nanostructures in the nanocomposite fibres as the influence of Cl ions also has been confirmed by the XRD pattern (Fig. 2 (A3)). The calcination process resulted in the transformation of nanocomposite ZnO fibers to ZnO nanoparticles. The possible reaction mechanisms with and without chloride ions are as follows:

$$[CH_2CH(OH)]_n + Zn(COOCH_3)_2 \cdot 2H_2O + H_2O \xrightarrow[\Delta]{} ZnO \downarrow + residues \uparrow \quad (4)$$

$$[CH_2CH(OH)]_n + Zn(COOCH_3)_2 \cdot 2H_2O + H_2O + HCl \xrightarrow[\Delta]{} ZnO \downarrow + residues \uparrow \quad (5)$$

Gilman *et al.*[33] have reported the decomposition of PVA into chain striping elimination of H_2O, residues of alcohol, methane, carbon (-CH(OH)-), aliphatic groups, non-protonated carbons and protonated sp3 carbons due to the intramolecular crystallization and radical reaction. During the calcination process, residual zinc oxide molecules in the composite fibers attained the required thermal energy with specific growth pattern to form ZnO nanospheres and nanorods. This can be explained with preferred nucleation and evolutionary selection growth mechanism.[34] In the early stage of calcination, nucleation driven by the surface energy minimization might have directed towards preferred orientation of crystallites. Further, principle of evolutionary selection (survival

of the fastest) model resulted in the growth ZnO nanostructures. In the evolutionary selection, the sticking coefficient of adatoms from the precursor and their energy corresponding to fastest growth resulted in the anisotropic crystal growth. The schematic representation of initial polymerization process followed by nucleation of hexagonal phase of ZnO during the calcination and the obtained nanostructures of ZnO are depicted in Fig. 3. Fig. 3b explicitly displays the adsorption of Zn atoms in the terminating polar phase of the crystal growth. The Cl ions in the precursor were profoundly adsorbed on to the surface than OH ions which in-turn act as capping agents to craftsmanship the ZnO nanorods. During the calcination process, the applied thermal energy distribution leads to the formation of ZnO molecules as a result of convection and diffusion initiated Zn^{2+} and O^{2-} ions movement. Further, the competition between OH^- and Cl^- ions has resulted in the different growth rate at different crystal planes. This is in good agreement with the report by Li *et al.*[35], where the velocities of ZnO crystal growth rates were described in the order V(001)>V(01$\bar{1}$)>V(010)>V(011>V(00$\bar{1}$).

Especially growth of ZnO nanorod can be explained in two ways (Fig. 4). Firstly, the isotropic kind of growth from its initial nucleation seed with a fixed crystal plane orientation. In this case the gowth of polar crystal face (001) in the c-axis. Secondly, a kind of anisotropic growth which is almost in all the direction of hexagonal plane of ZnO. Here the first type of growth might be due to the survival of fastest model[36] and the second might be emphasized to ligand effect.[35]

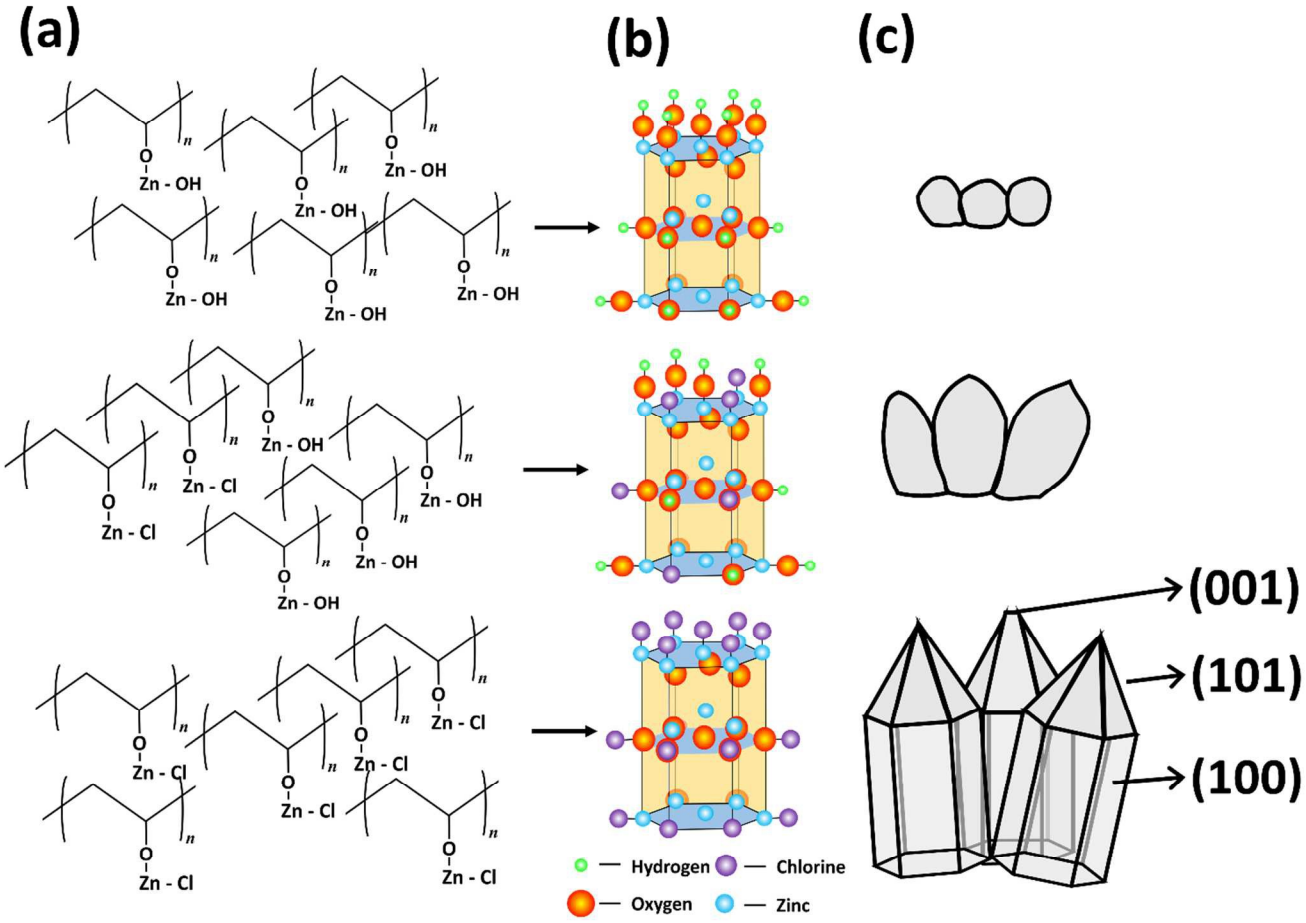

Fig. 3 Schematic model of the growth mechanism of ZnO nanostructures as a function of Cl ions concentrations.

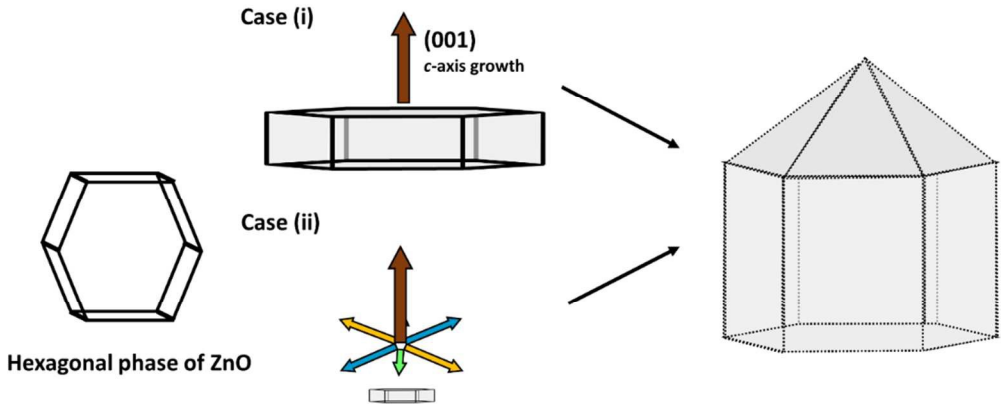

Fig. 4 Schematic representation of the growth mechanism of ZnO nanorods.

3.4 Electrical studies

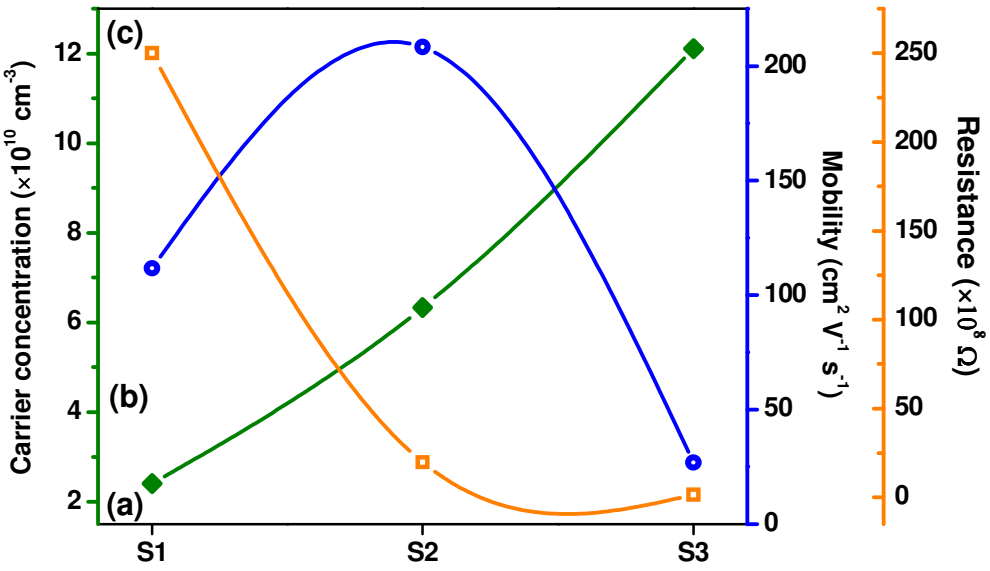

Fig. 5 (a) Carrier concentration, (b) mobility and (c) resistance of ZnO samples.

Fig. 5 shows the measured electrical properties namely carrier concentration, mobility and resistance of ZnO samples (S1, S2 and S3). The increase in carrier concentration from S1 to S3 clearly confirmed the phenomena of confinement of charge carriers in different types of nanostructures. The less number of carriers in nanospheres and increased concentration in nanorods have attributed to the size effect and their density of states. Also the increased number of native oxygen vacancies in ZnO nanorods might have resulted in the higher concentration. But the mobility of the nanorods (S3) was found to be lower than that of nanosphere (S1). This might be due to the effect of grain boundaries. In the case of S2, the higher mobility of 208 cm^2 $V^{-1}s^{-1}$ was observed. This may be due to the decreased crystalline defects and trapped density in the grain boundaries. Also the truncated trapezohedron shaped grain with well-connected grain boundaries might have resulted in a higher mobility. These observations have confirmed the

influence of band mobility, mean free path, free carrier concentration and trapped carriers at grain boundaries[37] on the electrical characteristics of ZnO. The measured resistance values were found to be lowest for the case of ZnO nanorods. This might be due to the highest carrier concentration. The variation in electrical characteristics is in same line with the observation made by Orton and Powell.[38]

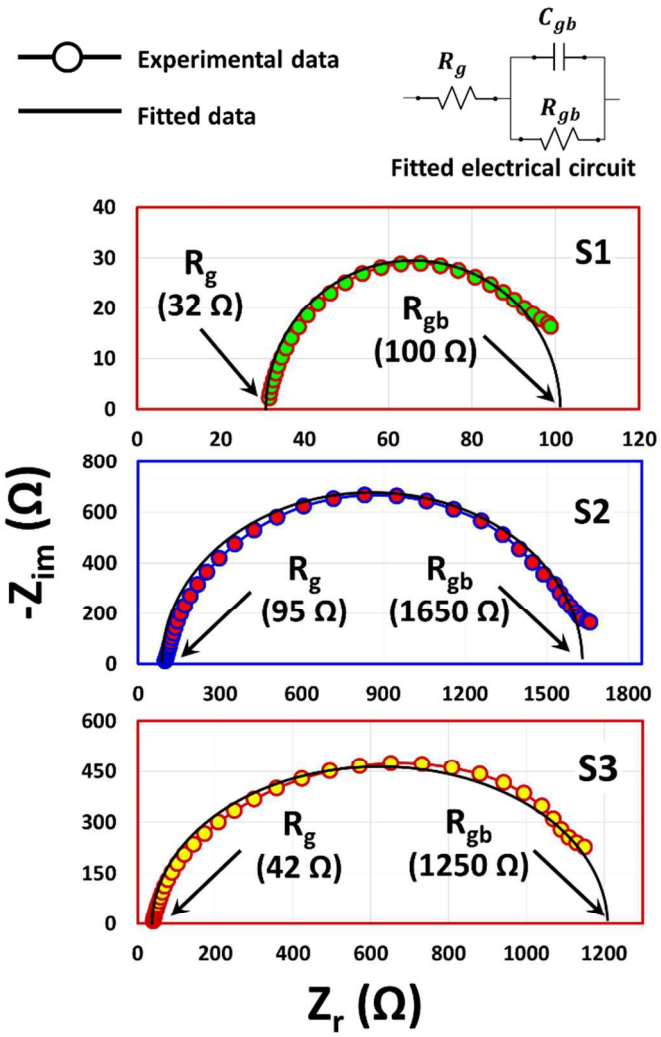

Fig. 6 Nyquist impedance plots for the ZnO samples S1, S2 and S3.

Since the current density depends on the grain size, shape, contact distribution, it is important to measure the grain and grain boundary resistances to analyze the transport mechanism. Hence the impedance spectroscopy measurements were made to observe the grain and grain boundary resistances of all the three samples (S1, S2 and S3). Fig. 6 shows the Nyquist impedance plot for the ZnO samples and the semi-circle arc is ascribed to grain resistance (R_g), grain boundary resistance (R_{gb}) and capacitance (C_{gb}) attributed from high to low frequencies. The shown equivalent electric circuit model reflects the contribution of grain and grain boundary resistances as well as the capacitance effect of grain boundary. The semicircle has exhibited the series connections of a contact resistance (R_g) and parallel combination of R_{gb} & C_{gb}. The calculated grain and grain boundary resistance were about 32, 95 and 42 Ω and 100, 1650 and 1250 Ω for S1, S2 and S3 samples respectively. The obtained values have confirmed the observed electrical characteristics of ZnO samples. This trend has reconfirmed the effect of morphology, grain size and shape, structural disorders, defects and vacancies[39] on the conductivity of the ZnO semiconducting material.

Fig. 7 depicts the Arrhenius plot of ZnO samples S1, S2 and S3. The temperature dependence of conductivity of the samples can be expressed in terms of conductance (G) which has been used to calculate the activation energy using the equation,

$$G = G_O \, exp\left(-\frac{\Delta E_a}{kT}\right) \quad (6)$$

where, G_O is a temperature independent factor, ΔE_a is the activation energy, k is the Boltzmann's constant and T is the absolute temperature. Activation energy or potential barrier at the grain boundary in the polycrystalline ZnO sample can be calculated from the slope of the Arrhenius

plot (ln(G) versus 1/T). The potential barrier values were be found to be 0.71, 0.623 and 0.718 eV for S1, S2 and S3 samples respectively. These values can be correlated with the inter-granular contact barrier height and different oxygen vacancies.[40] The existence of high mobility in S2 might have resulted in the low potential barrier height as compared to others.

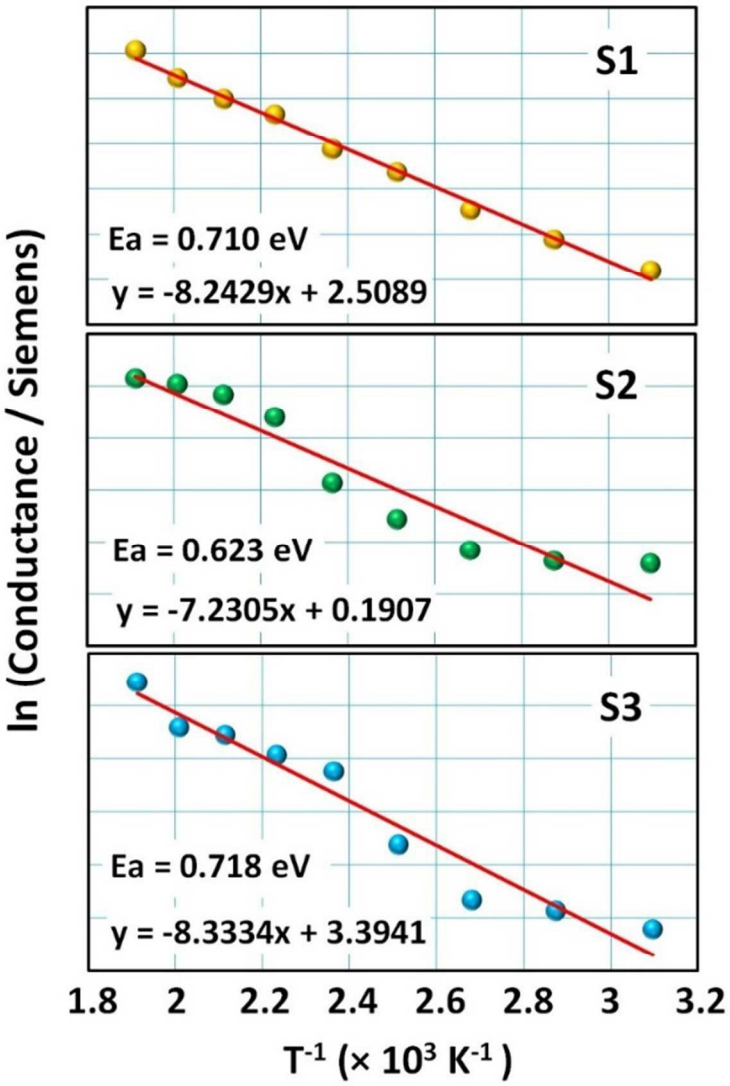

Fig. 7 Arrhenius plot for the ZnO sample S1, S2 and S3.

3.5 Sensing studies

The room temperature sensing characteristics of the obtained ZnO nanostructures were investigated using the sensing setup as shown in supplementary file (Fig. T2). Initially, the base line resistance of the *n*-type ZnO semiconductor was measured by exposing it to the air atmosphere. The gas (atmospheric oxygen)-solid (ZnO surface) interaction resulted in the formation of depletion layer in each grain due to the adsorption of conduction band electrons by oxygen molecules present in the atmosphere. In other words, adsorption of oxygen molecules on the surface of ZnO removes the electrons from its conduction band and increased the surface resistance. The reaction between oxygen and ZnO can be expressed as follows,

$$O_{2\,(atmosphere)} + e^-_{(ZnO\ surface)} \longrightarrow O^-_{2\,(ZnO)} \qquad (7)$$

Selectivity of the fabricated ZnO sensing elements was examined by exposing them to 100 ppm of various gases such as acetone, acetaldehyde, methanol and ethanol at the relative humidity of 54 % at room temperature. Fig. 8 shows the response of all the three fabricated samples towards all the gases. The response was found to be maximum for the sample S1 (60.90) towards ethanol.

Fig. 9(a) depicts the transient resistant response of ZnO sample (S1) with nanospherical morphology for 100 ppm of ethanol at room temperature and Fig. 9(b) shows the transient response of the sample (S1) for 5, 10, 50 and 100 ppm of ethanol. The sequential observation of transient response for various concentrations of ethanol showed the unchanged base line resistance which confirmed the repeatability of the sensing element.

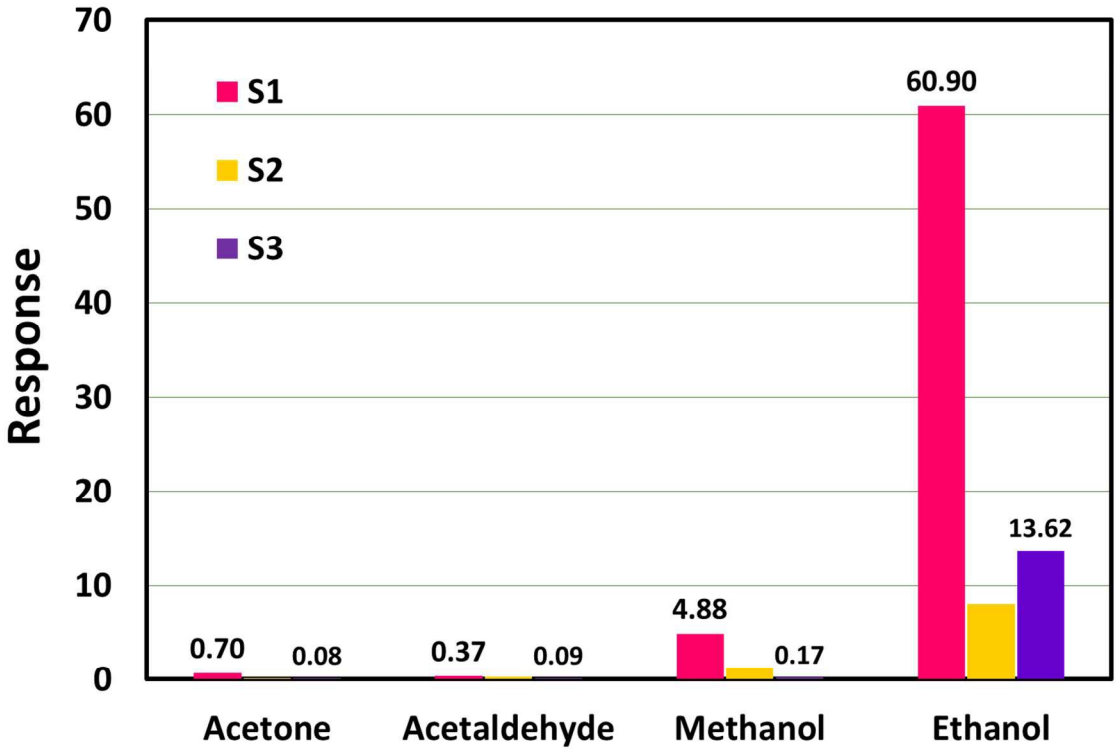

Fig. 8 Response of fabricated ZnO sensors (S1, S2 and S3) for 100 ppm of test gas (acetone, acetaldehyde, methanol and ethanol).

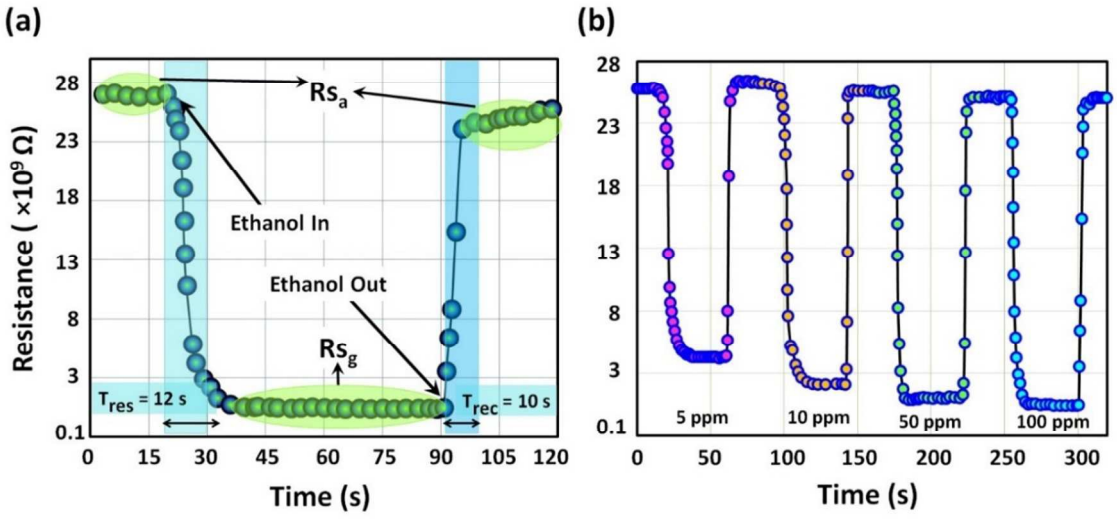

Fig. 9 Transient resistance response of sample (S1) towards (a) 100 ppm and (b) function of concentration (5, 10, 50 and 100 ppm) of ethanol.

3.5.1 Response and recovery times

Fig. 10 shows the trend of response and recovery times of the sample S1 for the various concentrations of ethanol. The response and recovery times were found to be in the range of 11-16 s and 8-10 s respectively. The response time increased with concentration and the recovery time decreased as expected.[41] It could be due to the increased number of reactive species acted on the sensor surface.

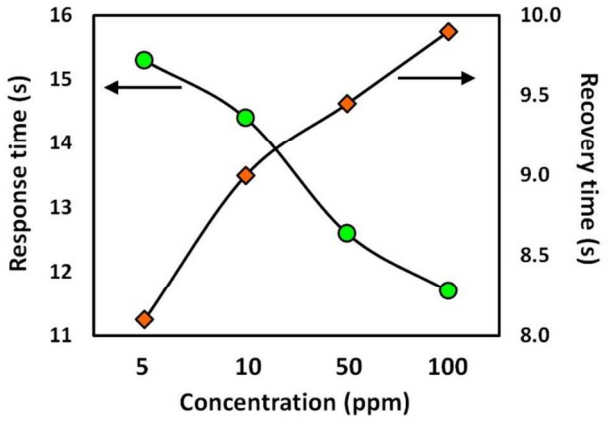

Fig. 10 Trend of response and recovery times of the sample S1 towards various concentration of ethanol.

3.5.2 Effect of humidity

Fig. 11 shows the response of sample S1 towards various concentrations of ethanol at different relative humidity levels. The humidity levels of 24%, 54% and 76% in ambient atmosphere was created by the saturated solutions of LiCl, MgCl, $MgNO_3$ and NaCl following the procedure reported elsewhere.[42] The standard hygrometer (HTC instruments, HD-306, India) was employed to measure the relative humidity in the sensing chamber. The resistance of the sensing element at 54% RH was 2.8×10^9 Ω, which increased to 5.4×10^9 Ω at lower RH (24%) and decreased to

0.52×10^9 Ω at higher RH (76%). The same trend was reported by Kannan *et al.*[43] as increase in relative humidity followed by decrease in resistance of *n*-type semiconductor.

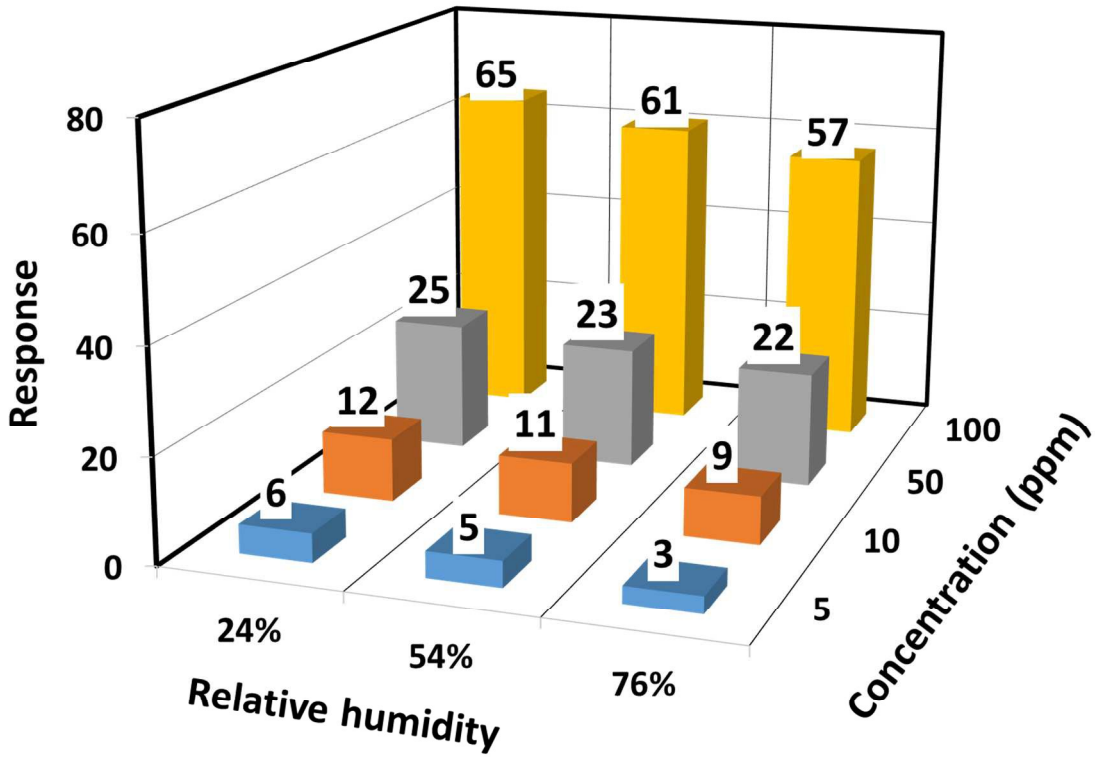

Fig. 11 Response of sample S1 towards various concentrations of ethanol at different humidity levels.

The responses toward higher concentrations of ethanol (Fig. 11) were found to be almost uniform at all humidity levels. But a considerable reduction in the response at higher humidity levels was observed for the lower concentrations of ethanol. This might be due to the impact of hopping and Grotthus transport mechanism.[44] At low humidity, chemisorption of hydroxyl ions lead to charge transport which can be explained by hopping mechanism. Further increase in

humidity level, physisorption of water molecules resulting in capillary condensation following the Grotthus transport mechanism.

3.5.3 Sensing mechanism

The overall sensing performance of the sensing element is decided by the receptor and transduction functions. The atmospheric oxygen sorption processes decide the base line resistance and the subsequent target gas molecules sorption processes decide the sensor response. But the final outcome is decided by the transduction function which, mainly depends on grain size, shape, grain resistance, grain boundary resistance or in other words morphology and inter granular contacts.

3.5.3.1 Receptor function

The gas-solid interaction before and after the formation of base line resistance especially between reducing gases such as acetone, acetaldehyde, methanol and ethanol and ZnO surface is presented in Eqs. 8-12. These equations clearly highlights the decrease in the surface resistance of ZnO with reference to base line resistance due to the oxidization of these gases on the surface of ZnO. During this process, the addition of electrons to the conduction band of ZnO by the concentration of reducing gases which in-turn proportional to the population density of adsorbed oxygen molecules on the surface of ZnO. Since this kind of sorption induced transient resistance response depends on the free charge carriers, their mobility and also the adsorption of oxygen molecules, kind of morphology, surface to volume ratio, surface catalytic activities play a decisive role in fixing the overall sensing performance of the sensing element. Among the three nanostructures, the spherical type showed the maximum response towards ethanol (Fig. 8).

Normally, ethanol vapour undergo dehydration and dehydrogenation reaction on the metal oxide surface based on the nature of surface as acidic or basic.[44,45] In this case, the basic oxide ZnO favoured the dehydrogenation reaction and Xu *et al.*[45] confirmed the enhanced sensing response due to the formation of acetaldehyde as an intermediate product when ZnO interacts with ethanol molecule.

Acetone [46] $CH_3COCH_3 + 4O^-_{2\,(adsorbed)} \longrightarrow 3CO_2 \uparrow + 3H_2O \uparrow + 4e^-$ (8)

Acetaldehyde [44] $2CH_3CHO + 5O^-_{2\,(adsorbed)} \longrightarrow 4CO_2 \uparrow + 4H_2O \uparrow + 5e^-$ (9)

Methanol [47] $CH_3OH + O^-_{2\,(adsorbed)} \longrightarrow HCOOH \uparrow + H_2O \uparrow + e^-$ (10)

Ethanol [44] (**Acidic oxide**) $C_2H_5OH \rightarrow C_2H_4 + H_2O \uparrow$ (11)

$C_2H_4 + 3O^-_{2\,(adsorbed)} \longrightarrow 2CO_2 \uparrow + 2H_2O \uparrow + 3e^-$

(**Basic oxide**) $2C_2H_5OH \rightarrow 2CH_3CHO + H_2 \uparrow$ (12)

$2CH_3CHO + 5O^-_{2\,(adsorbed)} \longrightarrow 4CO_2 \uparrow + 4H_2O \uparrow + 5e^-$

Also, bond-dissociation energy (BDE)[48] and dipole moment[49] of the gas molecules play a significant role in adsorption/desorption on the surface and resulting in specific response of the sensor (Table 2). The transfer of energy from sensor surface to oxygen and target gas molecules to dissociate or decompose happens by transfer of electrons. Hence, selectivity of the sensor depends upon the surface energy which can be based on the morphology of the sensor element. Generally, unequal distribution of electrons in the molecule exhibits a polar behaviour which results in dipole moment. Normally, alcohol group exhibits lesser dipole moment and higher

polar nature than aldehydes and ketones. Thus highly sensitive and selective response towards ethanol molecule might be due to high BDE and low dipole moment than other target molecules.

Table 2 Bond-dissociation energy, dipole moment and response of the sensor S1 towards 100 ppm of samples.

Sample	**Bond-dissociation energy (kJ mol^{-1})**	**Dipole moment (D)**	**Sensitivity of sensor S1 (%) (100 ppm)**
Acetone	393.0	2.88	0.70
Acetaldehyde	364.0	2.70	0.37
Methanol	436.8	1.70	4.88
Ethanol	436.0	1.69	60.90

3.5.3.2 Transduction fuction

In metal oxide semiconductor gas sensors, grains and grain boundaries are pivotal factors for the change in surface resistance as well as response. In receptor function, adsorbed oxygen ions trap the electrons in the grains and create depletion layer in the boundaries, which results in the increase of the width of space charge region.[50] Further, interaction with reducing gases results in the increase in electron concentration in-turn decrease the width of space charge region. This leads to increase and decrease of the grain and grain boundary resistances and hence the potential barrier between two grains.[39] Moreover, the obtained electrical signal by chemical interaction is transduced through the granular coagulated particles in the polycrystalline sensing element like ZnO.[51] Each granular particles are connected with one another by grain boundary contacts and established a percolation path for the conduction of electrons. This can be governed by the mobility of carriers, carrier density and scattering centres in grains and spatial arrangement of

grain boundaries and their contact area. Hence transfer of electrons between grains can be achieved by overcoming the surface potential barrier at each boundary and also the formed width of space-charge layer (or depletion layer) inside the granular particles.

Ihokura and Mitsudo have pointed out that change in potential barrier height and space-charge layer width at each grain boundary and grain corresponds to gas-dependent resistance of the sensor element.[51] Thus, width of the space charge region can be correlated with the observed grain boundary resistance[52] and potential barrier height as a inter granular activation energy.[53]

In the present investigation, the spherical shaped ZnO (S1) showed better response towards ethanol due to lesser grain and grain boundary resistances with lower depletion width and of 0.71 eV as barrier height. But the other two samples (S2 and S3) showed lower response than S1 and the same trend is in accordance with the observed electrical parameters. Furthermore, the sensor S1 has followed grain boundary-control model whereas S2 and S3 obeyed the neck-control model as proposed by Yamazoe *et al.*[52]. The schematic representation shown in Fig. 12, clearly depicts the morphology based space charge model and potential barrier height model which decide the transduction property of the sensing element. The observed sensing response of ~60.90 towards 100 ppm of ethanol in room temperature (300 K) has been the best with reference the latest reports available in literature (Table 3).

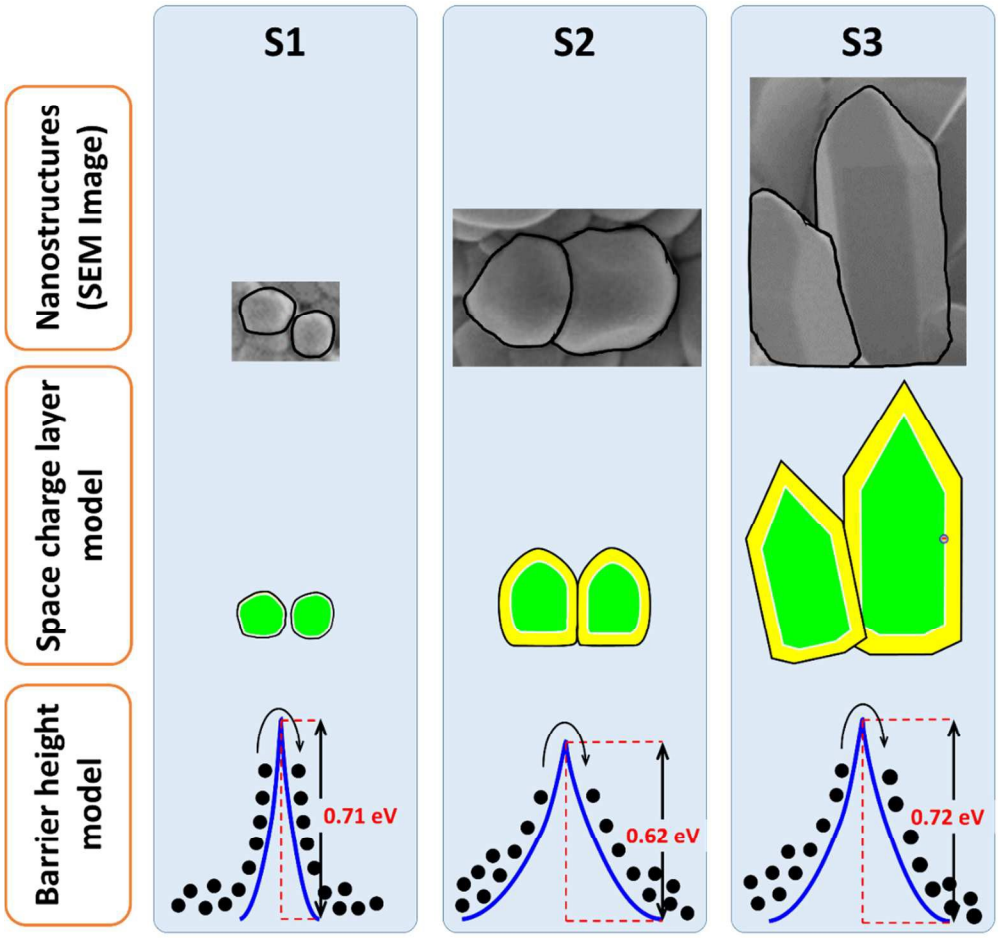

Fig. 12 Schematic representation shown the morphology, space charge model and potential barrier height model to exhibit the transduction property of the sensor.

Table 3 Comparison of sensing response of ZnO sensor with different morphology at room temperature**.**

ZnO morphology	**Concentration (ppm)**	**Sensitivity (%)**	**Reference**
Nanosphere	**100**	**60.9**	**Present work**
Nanosphere	50	2.73	[54]
Nanosphere	100	1.80	[55]
Nanoflakes	200	Appreciable	[56]

4 Conclusion

ZnO nanospheres and nanorods were successfully grown using electrospinning technique. A facile and template free method of growing nanorods by varying the Cl ion concentration in precursor as capping agent has been developed. This novel approach can be used to engineer the nanostructures of ZnO with desired transport properties. The role of morphology, mobility, carrier concentration, activation energy, grain and grain boundary resistances of the ZnO nanostructures on their sensing pattern has been highlighted. The obtained figure of merits of the room temperature ethanol sensor found to be predominant with reference to the sensors reported in the literature.

Acknowledgements

The authors wish to express their sincere thanks to Department of Science & Technology, New Delhi, India for their financial support through IDP (IDP/IND/2012/41(General)) and FIST (SR/FST/ETI-284/2011(C)), and also the Nano Mission Council, Government of India (SR/NM/PG-16/2007). We also wish to acknowledge SASTRA University, Thanjavur for extending infrastructure support to carry out this work.

References

1 L. Schmidt-mende and J. L. Macmanus-driscoll, *Mater. Today*, 2007, **10**, 40–48.

2 B. Weintraub, Z. Zhou, Y. Li and Y. Deng, *Nanoscale*, 2010, **2**, 1573–1587.

3 E. Manikandan, J. Kennedy, G. Kavitha, K. Kaviyarasu, M. Maaza, B. K. Panigrahi and U. K. Mudali, *J. Alloys Compd.*, 2015, **647**, 141–145.

4 S. Xu and Z. L. Wang, *Nano Res.*, 2011, **4**, 1013–1098.

5 Z. L. Wang, *Mater. Today*, 2004, **7**, 26–33.

6 Y. Zhang, M. K. Ram, E. K. Stefanakos and D. Y. Goswami, *J. Nanomater.*, 2012, **2012**.

7 Z. L. Wang, *Chinese Sci. Bull.*, 2009, **54**, 4021–4034.

8 X. Gan, X. Li, X. Gao and W. Yu, *J. Alloys Compd.*, 2009, **481**, 397–401.

9 N. Kilinc, O. Cakmak, A. Kosemen, E. Ermek, S. Ozturk, Y. Yerli, Z. Z. Ozturk and H. Urey, *Sensors Actuators, B Chem.*, 2014, **202**, 357–364.

10 Q. Zhang, S.-J. Liu and S.-H. Yu, *J. Mater. Chem.*, 2009, **19**, 191.

11 T. Dedova, O. Volobujeva, J. Klauson, A. Mere and M. Krunks, *Nanoscale Res. Lett.*, 2007, **2**, 391–396.

12 R. H. Zhang, E. B. Slamovich and C. a Handwerker, *Nanotechnology*, 2013, **24**, 195603.

13 I. Singh, G. Kaur and R. K. Bedi, *Appl. Surf. Sci.*, 2011, **257**, 9546–9554.

14 M. Huang, Y. Yan, W. Feng, S. Weng, Z. Zheng, X. Fu and P. Liu, *Cryst. Growth Des.*, 2014, **14**, 2179–2186.

15 A. Smith, J.-M. Laurent, D. S. Smith, J.-P. Bonnet and R. R. Clemente, *Thin Solid Films*, 1995, **266**, 20–30.

16 M. Krunks, T. Dedova, E. Karber, V. Mikli, I. O. Acik, M. Grossberg and A. Mere, *Phys. B*, 2009, **404**, 4422–4425.

17 G. K. Mani and J. B. B. Rayappan, *RSC Adv.*, 2015, **5**, 54952–54962.

18 J. Zhu, G. Zhang, S. Gu and B. Lu, *Electrochim. Acta*, 2014, **150**, 308–313.

19 Y. Li, X.-Y. Yang, Y. Feng, Z.-Y. Yuan and B.-L. Su, *Crit. Rev. Solid State Mater. Sci.*, 2012, **37**, 1–74.

20 J. Zhang, S. Wang, M. Xu, Y. Wang, B. Zhu, S. Zhang, W. Huang and S. Wu, *Cryst. Growth Des.*, 2009, **9**, 3532–3537.

21 G. K. Mani and J. B. B. Rayappan, *RSC Adv.*, 2014, **6**, 64075.

22 N. Bhardwaj and S. C. Kundu, *Biotechnol. Adv.*, 2010, **28**, 325–347.

23 A. Baji, Y. W. Mai, S. C. Wong, M. Abtahi and P. Chen, *Compos. Sci. Technol.*, 2010, **70**, 703–718.

24 B. Caratão, E. Carneiro, P. Sá, B. Almeida and S. Carvalho, *J. Nanotechnol.*, 2014, **2014**, 472132(5pp).

25 C. Zhu, B. Lu, Q. Su, E. Xie and W. Lan, *Nanoscale*, 2012, **4**, 3060.

26 W. Li, S. Ma, Y. Li, G. Yang, Y. Mao, J. Luo, D. Gengzang, X. Xu and S. Yan, *Sensors Actuators, B Chem.*, 2015, **211**, 392–402.

27 B. Huang, C. Zhao, M. Zhang, Z. Zhang, E. Xie, J. Zhou and W. Han, *Appl. Surf. Sci.*, 2015, **349**, 615–621.

28 M. I. Abd-Elrahman, *Nanoscale Microscale Thermophys. Eng.*, 2013, **17**, 194–203.

29 X. Yu, F. Song, B. Zhai, C. Zheng and Y. Wang, *Phys. E Low-Dimensional Syst. Nanostructures*, 2013, **52**, 92–96.

30 S. Baruah, M. A. Mahmood, M. T. Z. Myint, T. Bora and J. Dutta, *Beilstein J. Nanotechnol.*, 2010, **1**, 14–20.

31 R. K. N. B, V. Crasta, R. F. Bhajantri and B. M. Praveen, *J. Polym.*, 2014, **2014**, 846140(7pp).

32 L. Motevalizadeh, Z. Heidary and M. E. Abrishami, *Bull. Mater. Sci.*, 2014, **37**, 397–405.

33 J. W. Gilman, D. L. VanderHart and T. Kashiwagi, in *Fire and Polymers II*, 1995, vol. 6, pp. 415–424.

34 D. Köhl, G. Natarajan and M. Wuttig, *J. Phys. D. Appl. Phys.*, 2012, **45**, 245302.

35 W.-J. Li, E.-W. Shi, W.-Z. Zhong and Z.-W. Yin, *J. Cryst. Growth*, 1999, **203**, 186–196.

36 A. Van der Drift, *Philips Res. Rep*, 1967, **22**, 267–288.

37 S.-J. Chang, M. Cheralathan, M. Bawedin, B. Iniguez, B. Bayraktaroglu, J.-H. Lee, J.-H. Lee and S. Cristoloveanu, *Solid. State. Electron.*, 2013, **90**, 134–142.

38 J. W. Orton and M. J. Powell, *Reports Prog. Phys.*, 2000, **43**, 1263–1307.

39 F. Ren, L. Huang, Y. Ling and J. Feng, *Sensors Actuators, B Chem.*, 2010, **148**, 195–199.

40 N. Kakati, S. H. Jee, S. H. Kim, J. Y. Oh and Y. S. Yoon, *Thin Solid Films*, 2010, **519**, 494–498.

41 S. M. Kanan, O. M. El-Kadri, I. a. Abu-Yousef and M. C. Kanan, *Sensors*, 2009, **9**, 8158–8196.

42 G. K. Mani and J. B. B. Rayappan, *Sensors Actuators, B Chem.*, 2013, **183**, 459–466.

43 P. K. Kannan, R. Saraswathi and J. B. B. Rayappan, *Sensors Actuators, A Phys.*, 2010, **164**, 8–14.

44 P. Shankar and J. B. B. Rayappan, *Sci. Lett.*, 2015, **4**, 126.

45 J. Xu, J. Han, Y. Zhang, Y. Sun and B. Xie, *Sensors Actuators, B Chem.*, 2008, **132**, 334–339.

46 S. S. Nath, M. Choudhury, D. Chakdar, G. Gope and R. K. Nath, *Sensors Actuators, B Chem.*, 2010, **148**, 353–357.

47 P. P. Sahay and R. K. Nath, *Sensors Actuators, B Chem.*, 2008, **134**, 654–659.

48 G. K. Mani and J. B. B. Rayappan, *Sensors Actuators, B Chem.*, 2014, **198**, 125–133.

49 L. Wang, K. Kalyanasundaram, M. Stanacevic and P. Gouma, *Sens. Lett.*, 2010, **8**, 709–712.

50 A. Labidi, C. Jacolin, M. Bendahan, A. Abdelghani, J. Guérin, K. Aguir and M. Maaref, *Sensors Actuators, B Chem.*, 2005, **106**, 713–718.

51 N. Yamazoe, *Sensors Actuators, B Chem.*, 1991, **5**, 7–19.

52 C. Xu, J. Tamaki, N. Miura and N. Yamazoe, *Sensors Actuators, B Chem.*, 1991, **3**, 147–155.

53 M. A. Alim, S. Li, F. Liu and P. Cheng, *Phys. Status Solidi Appl. Mater. Sci.*, 2006, **203**, 410–427.

54 P. Shankar and J. B. B. Rayappan, *Sens. Lett.*, 2013, **11**, 1956–1959.

55 X. Zhou, Q. Xue, H. Chen and C. Liu, *Phys. E*, 2010, **42**, 2021–2025.

56 H. J. Pandya, S. Chandra and A. L. Vyas, *Sensors Actuators, B Chem.*, 2012, **161**, 923–928.

Figure captions

Fig. 1 FE-SEM images of as-deposited ZnO nanofibers (A1, A2 &A3) and calcined samples (S1, S2 & S3), (Inset in S3: Magnified single nanorod).

Fig. 2 XRD patterns of as-deposited ZnO nanofibers (A1, A2 & A3) and calcined samples (S1, S2 & S3).

Fig. 3 Schematic model of the growth mechanism of ZnO nanostructures as a function of Cl ions concentrations.

Fig. 4 Schematic representation of the growth mechanism of ZnO nanorods.

Fig. 5 (a) Carrier concentration, (b) mobility and (c) resistance of ZnO samples.

Fig. 6 Nyquist impedance plots for the ZnO samples S1, S2 and S3.

Fig. 7 Arrhenius plot for the ZnO sample S1, S2 and S3.

Fig. 8 Response of fabricated ZnO sensors (S1, S2 and S3) for 100 ppm of test gas (acetone, acetaldehyde, methanol and ethanol).

Fig. 9 Transient resistance response of sample (S1) towards (a) 100 ppm and (b) function of concentration (5, 10, 50 and 100 ppm) of ethanol.

Fig. 10 Trend of response and recovery times of the sample S1 towards various concentration of ethanol.

Fig. 11 Response of sample S1 towards various concentrations of ethanol at different humidity levels.

Fig. 12 Schematic representation shown the morphology, space charge model and potential barrier height model to exhibit the transduction property of the sensor.

Table captions

Table 1. Calculated lattice parameters for the calcined samples.

Table 2 Bond-dissociation energy, dipole moment and response of the sensor S1 towards 100 ppm of samples.

Table 3 Comparison of sensing response of ZnO sensor with different morphology at room temperature**.**